J Geod (2006) 80: 204–216
DOI 10.1007/s00190-006-0052-x

ORIGINAL ARTICLE

Cheinway Hwang · Jinyun Guo · Xiaoli Deng
Hsin-Ying Hsu · Yuting Liu

Coastal gravity anomalies from retracked Geosat/GM altimetry: improvement, limitation and the role of airborne gravity data

Received: 20 September 2005 / Accepted: 27 April 2006 / Published online: 30 May 2006
© Springer-Verlag 2006

Abstract We process geophysical and waveform data records of the Geosat/GM (geodetic mission) satellite altimeter mission for waveform retracking and applications. An improved threshold retracker is developed. The performances of the Beta-5, threshold and improved threshold retrackers are assessed over waters around Taiwan. The improved threshold retracker outperforms the other two. The improvement in the accuracy of sea surface height (SSH) is investigated according to marine zone and the distance of waters to the shore. The improvement rate increases closer to the land, with the largest improvement rate of about 20% in waters within 10 km of the shore. Over waters around islands and coasts, there are still retracked SSHs with large errors. Least-squares collocation is used to compute gravity anomalies from the Geosat/GM altimeter data. Use of retracked SSHs improves the accuracy of gravity anomalies by about 11%. Adding airborne gravity data further improves the accuracy, especially in the immediate vicinity of the coasts. Tide model errors over coastal waters remain a problem in altimetry applications, even if the waveforms are properly retracked.

C. Hwang (✉) · J. Guo · H.-Y. Hsu, Y. Liu
Department of Civil Engineering, National Chiao Tung University,
1001 Ta Hsueh Road, Hsinchu, Taiwan
E-mail: hwang@geodesy.cv.nctu.edu.tw
Tel.: +886-3-5724739
Fax: +886-3-5716257

J. Guo
Department of Surveying and Land Information,
Xuzhou Normal University, 29 Shanghai Road,
Xuzhou, 221116, China
E-mail: guojy@geodesy.cv.nctu.edu.tw
Tel.:+886-3-5724739
Fax: +886-3-5716257

X. Deng
Discipline of Civil, Surveying and Environmental Engineering,
School of Engineering, The University of Newcastle,
University Drive, Callaghan, NSW 2308, Australia
E-mail: xiaoli.deng@newcastle.edu.au
Tel.: +61-2-49216039
Fax: +61-2-49216991

Keywords Geosat/GM · Gravity anomaly · Waveform retracking · Taiwan · Tide model error

1 Introduction

Most marine applications of satellite altimetry begin with sea surface heights (SSH). ANSSH from altimetry is derived from the satellite's orbital height, and the range between the antenna and the sea surface determined using the waveforms of the altimeter. Over the deep oceans without land interference, the waveforms created by the returning altimeter pulse generally follow the ocean model of Brown (1977), and the corresponding range can be properly determined using the result from an onboard tracker. Near coasts, altimeter waveforms may be corrupted due to a variety of reasons so that the range observations can be in error. For example, such corruptions of waveforms in ERS and Envisat altimetry over global coastal zones have been presented by Mathers et al. (2004). Use of erroneous altimeter ranges may lead to false results in such applications as gravity anomaly determination and sea-level change studies.

Recent efforts by, e.g., Smith and Sandwell (2004) and Andersen et al. (2005) have shown that the use of retracked SSHs can improve the determination of gravity anomalies over coastal waters and the open ocean. A retracked SSH here is defined as a SSH which, in addition to standard geophysical and instrument corrections (Fu and Cazenave 2001), is corrected by the tracking gate bias determined from waveform retracking. Altimeter waveform corruption can be in various forms, depending on the altimeter and the geographic location. For example, Deng et al. (2002) estimated that TOPEX/Poseidon (T/P) waveforms are corrupted over waters about 20 km from the shore around southern Australia. Waveform corruptions over ice and land are in different patterns to those over coastal waters, requiring different algorithms for proper retracking.

Methods of waveform retracking may be classified into two categories: one is based on functional fit and the other based on statistics. A review of waveform retracking methods

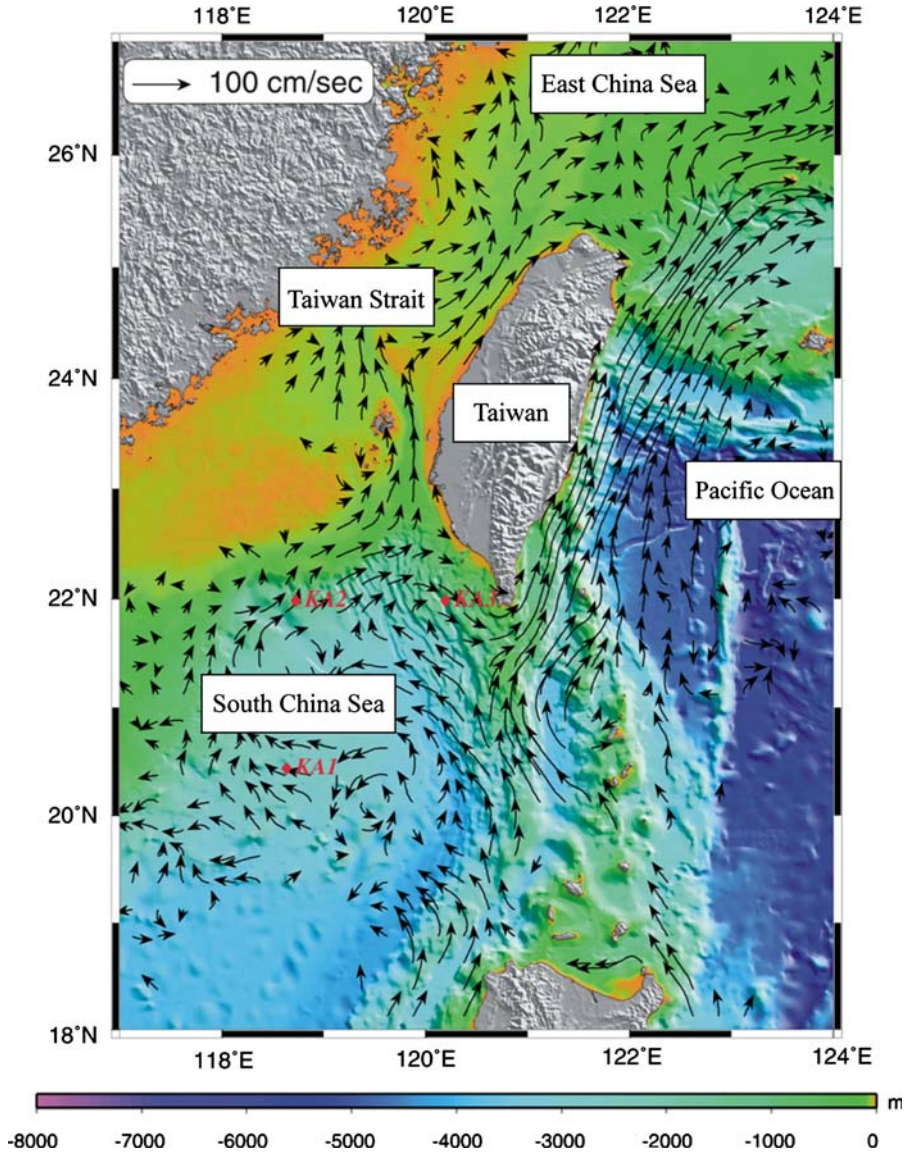

Fig. 1 Bathymetry and coastal geometry around Taiwan, vectors show mean ocean current velocities. The Kuroshio Current dominates the velocity field east of Taiwan (adapted from National Center for Ocean Research, Taiwan, http://www.ncor.ntu.edu.tw with permission)

can be found in, e.g., Deng (2004) and Zwally and Brenner (2001). The goal of this study is to develop an improved method for retracking Geosat/GM (geodetic mission) altimeter waveforms and assess the extent of improvement that this method can achieve. We will focus on just one recipe of retracking based on our available resources, and we have no intention to assess the performance of all retrackers available in the scientific community. As an application of the retracked Geosat/GM altimetry, gravity anomalies will be derived from retracked SSHs of Geosat/GM and their quality will be assessed.

The area chosen for our experiments is over the waters around Taiwan. The bathymetry and coastal geometry here are rather diverse (Fig. 1). East of Taiwan, the collision of the Eurasia Plate and the Philippine Sea Plate creates islands and complex shorelines. Here, the depth of the Pacific Ocean plunges to 4 km just about 10 to 20 km off the east coast of Taiwan. West of Taiwan lies the Taiwan Strait, where the deepest part is only 50 m and the sea is scattered with islands and barrier islands. Less than 200 m in depth, the East China Sea lies north of Taiwan and is also scattered with islands near Taiwan. The South China Sea is south of Taiwan and, here, a small island called Liuchou might interfere with altimeter waveforms.

Given the varying depths and the complicated coastal geometry around Taiwan, different degrees of waveform corruption are expected. In addition, the roughness of the gravity field around Taiwan varies from one area to another: it is smooth over the Taiwan Strait, the East China Sea and the South China Sea (range of gravity anomaly variation: tens of

mgal) and it is rough over the Pacific Ocean (range of gravity anomaly variation: hundreds of mgal). Ocean tides in the Taiwan Strait are complicated, with large tidal amplitudes near the coasts of the mainland China and Taiwan (Jan et al. 2004). As such, we expect large remaining errors in altimetry due to tide model error, even after altimeter ranges are properly corrected by retracking.

The well-edited shipborne gravity data from Hsu et al. (1998) make it possible to assess the accuracy of altimeter-derived gravity anomalies around Taiwan. Furthermore, airborne gravity data are available (C. Hwang et al., submitted) and can be used to investigate (1) whether adding airborne gravity data to altimeter data will enhance the accuracy of altimeter-derived gravity anomalies, and (2) to assess the accuracy of altimeter-only gravity anomalies over regions of different depths, including the immediate vicinity of the coasts.

2 Geophysical and waveform data records of Geosat/GM

The data needed for this work are the products of the Geosat/GM mission, including the Geophysical Data Records (GDRs), Sensor Data Records (SDRs) and Waveform Data Records (WDRs). These data were supplied by the National Oceanic and Atmospheric Administration (NOAA); see Cheney et al. (1991) and Lillibridge et al. (2004) for the descriptions of Geosat/GM GDRs, SDRs and WDRs. One day of Geosat/GM GDRs are stored in one file and the data set spans from day 90 of 1985 to day 273 of 1986, resulting in a total of 549 days and files, respectively. In one GDR record, there are 78 bytes of information containing 34 parameters, including geophysical corrections at 1 Hz. Near coasts and over land, missing GDRs are frequent due to loss of altimeter lock. In contrast, half day of WDRs are stored in one file. Each WDR contains 660 bytes of information, but only including radar return waveform samples for each of the 63 altimeter gates at 10 Hz. To avoid such problems as thermal noise, only 60 effective gate values are used for retracking.

The SDR product contains the raw measurements and onboard computed parameters. Each SDR also spans a 24-h measurement period from midnight to midnight (cf. Cole 1985). The GDR product is tied to the SDR and WDR products using a common time frame described subsequently. First, the time format associated with a GDR is Coordinated Universal Time (UTC), while a Geosat-A Telemetry Stream time format is associated with both the SDR and WDR. Following the telemetry stream definition, a frame count (FC) is computed as (Cole 1985)

$$\mathrm{FC} = 32 \times \mathrm{MFC} + \mathrm{mFC} \tag{1}$$

where MFC is the major frame count and mFC is the minor frame count, both available on SDRs and WDRs. In this study, we convert UTC of GDRs to FC as (Cole 1985)

$$\mathrm{FC\_GDR} = \mathrm{int}\left(\mathrm{FC0} + \frac{\mathrm{s85} - \mathrm{epoch\_s85} - 0.005 - 4.4}{\mathrm{sec\_per\_fc}}\right) \tag{2}$$

where FC_GDR is the FC associated with a UTC (s85), int stands for the integer part, FC0 is the beginning count of FC in a day, epoch_s85 is 0 h UTC of a day and sec *_per_fc* is the time span of a FC.

This results in a consistent time frame for properly extracting geophysical corrections and other information from GDRs by linear interpolation, which are then combined with the range corrections from the retracking of waveforms in the WDRs. The geophysical corrections applied to the Geosat/GM instantaneous SSHs include solid-Earth and ocean tides, tropospheric and ionospheric delays, pole tide, inverse barometer effect and sea state bias. For gravity derivation, we reduce the sampling rate to 2 Hz by fitting a degree-2 polynomial to the 10 Hz, retracked SSHs without smoothing.

3 Retracking Geosat/GM waveforms

3.1 Selected methods of waveform retracking

Waveforms are a series of powers at altimeter gates generated by a returning pulse from the sea. In the open ocean, waveforms are assumed to follow the functional form of Brown (1977), called ocean waveforms, and the corresponding range between the antenna and the sea is derived from an onboard tracker based on such waveforms. The tracker works in a window of waveforms. The tracking gate within the window determines the time for calculating the range.

For the ocean mode, the tracking gate is set to be at the center point of the leading edge. For example, Fig. 2 shows 20 waveforms of Geosat/GM along track 85282 (Fig. 3). The waveforms in Fig. 2 start from the west coast of Taiwan and end in the Taiwan Strait. Waveforms 13–20 (those away from the coast) generally follow the Brown model, but waveforms 1–12 (those close to the coast) differ from the Brown model significantly. The reason is that the surface geometry and reflecting properties near the coast deviate from those over the open ocean, leading to distorted waveforms. Furthermore, Fig. 2 shows that for both the ocean and non-ocean waveforms, the pre-defined tracking gate of 30.5 does not match the leading edges of waveforms 1–20 in most cases. Thus, retracking is required for both types of waveform.

There are numerous methods for waveform retracking. In this paper, we will experiment with four methods that are both based on functional fit and statistics. For the method of functional fit, we chose to use the Beta-5 retracker (Martin et al. 1983; Anzenhofer et al. 1999), which fits waveforms by the function

$$y_t = \beta_1 + \beta_2(1 + \beta_5 Q)p\left(\frac{t - \beta_3}{\beta_4}\right) \tag{3}$$

with

$$Q = \begin{cases} 0 & \text{for } t < \beta_3 + 0.5\beta_4 \\ t - (\beta_3 + 0.5\beta_4) & \text{for } t \geq \beta_3 + 0.5\beta_4 \end{cases} \tag{4}$$

$$p(x) = \frac{1}{\sqrt{2\pi}} \int_{-\infty}^{x} \exp\left(\frac{-q^2}{2}\right) dq \tag{5}$$

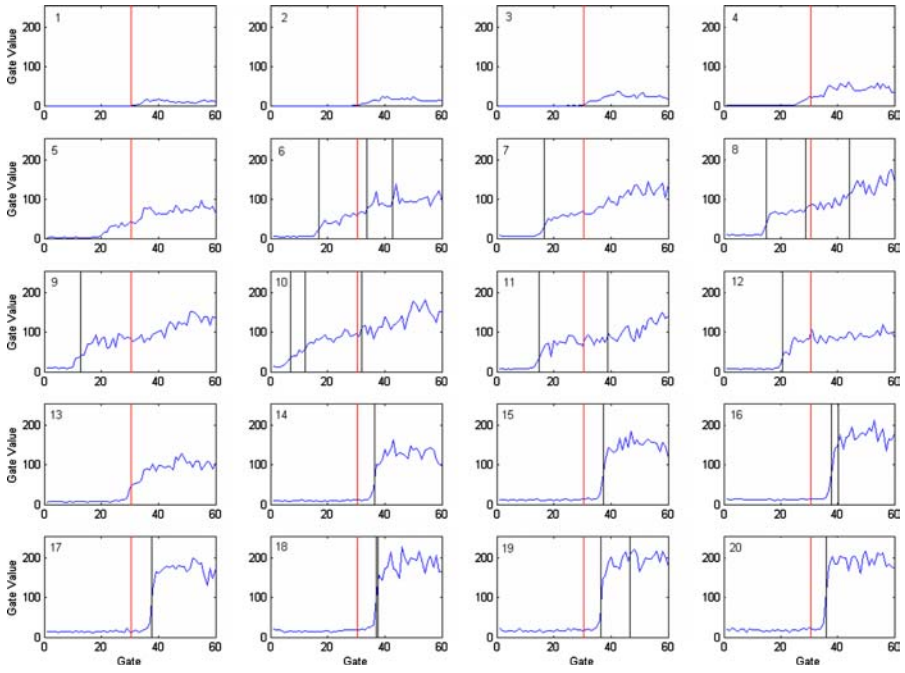

Fig. 2 Ground tracks of Geosat/GM 85206 and 85282

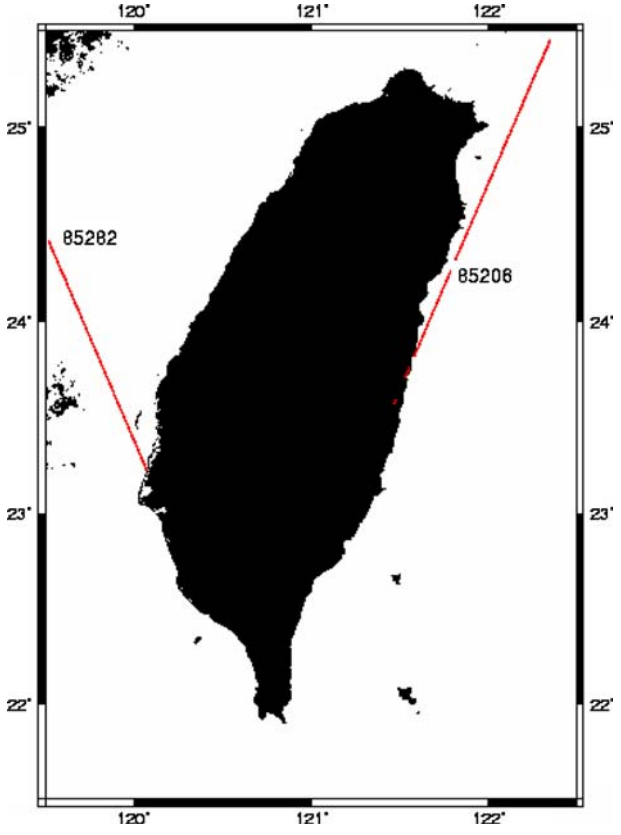

Fig. 3 Waveforms along track 85282; the waveform sequence starts from west coast of Taiwan and end in the Taiwan Strait

where q is the variable of the normal distribution function $\exp(-q^2/2)$, y_t is the power at gate t(t ranges from 1 to 60 for Geosat/GM), β_1 is thermal noise, β_2 is the amplitude, β_3 is the gate corresponding to the center of the leading edge (retracking gate), β_4 is the half ascending time of the leading edge, and β_5 is the slope of the trailing edge.

The five parameters can be determined using least-squares. Anzenhofer et al. (1999) give details of the associated partial derivatives and a weighting scheme in the least-squares solution for the Beta-5 retracker. For the Beta-5 retracker used in this paper, we adopt the solution scheme of Anzenhofer et al. (1999). The correction due to retracking is computed by

$$\Delta \mathrm{R} = 0.46875\,(\beta_3 - 30.5)\ \mathrm{m} \tag{6}$$

As for the statistics-based methods, we experimented with a variant of the offset center of gravity (OCOG) method developed by Wingham et al. (1986) and a modified version of the threshold retracking developed by Davis (1997). In Section 3.2, we will present an improved method of retracking. The OCOG method estimates the amplitude, width and center of gravity (COG) of waveforms using the formulae

$$A = \sqrt{\sum_{t=1+n}^{60-n} y_t^4 \Big/ \sum_{t=1+n}^{60-n} y_t^2} \tag{7}$$

$$W = \left(\sum_{t=1+n}^{60-n} y_t^2\right)^2 \Big/ \sum_{t=1+n}^{60-n} y_t^4 \tag{8}$$

$$\mathrm{COG} = \sum_{t=1+n}^{60-n} t y_t^2 \Big/ \sum_{t=1+n}^{60-n} y_t^2 \tag{9}$$

$$G^r_{\mathrm{ocog}} = \mathrm{COG} - \frac{W}{2} \tag{10}$$

where y_t is the same as in Eq. (3), A is amplitude [equivalent to β_2 in Eq. (3)], W is width, COG is the gate of center of

gravity of waveforms, and G^r_{ocog} is the retracking gate [equivalent to β_3 in Eq. (3)]. In this method, we have excluded powers at the first and last n gates (n is set to 4 in this paper), which might contain large noises and damage the solution.

The estimates of waveform parameters from OCOG can be used as a priori values in the least-squares solution of the Beta-5 retracker. It can also be used to classify waveforms and to estimate waveform quality (Anzenhofer et al. 1999). In comparison to the Beta-5 retracker, the OCOG retracker is easy to implement on a computer. While there is no guarantee of convergence in the least-squares solution of the Beta-5 retracker, the OCOG retracker will always deliver a solution. However, the OCOG may not produce accurate range correction for coastal altimeter measurements, because it cannot centre at the leading edge of the distorted waveforms (Deng et al. 2002).

Another statistics-based method to be assessed is a modified threshold retracking. This method employs a threshold value to determine the retracking gate.

The formulae we use are

$$y_N = \frac{1}{5}\sum_{i=1}^{5} y_i \tag{11}$$

$$T_l = \alpha(A - y_N) + y_N \tag{12}$$

$$G^r_{\text{thr}} = G_{k-1} + \frac{T_l - y_{k-1}}{y_k - y_{k-1}}(G_k - G_{k-1}) \tag{13}$$

where A is determined by Eq. (7), y_N is the averaged value of the first five powers, α is a threshold value, G_k is kth gate whose power is greater than T_l, and G^r_{thr} is the retracking gate (equivalent to β_3 and G^r_{ocog}). If y_k equals y_{k-1}, then k is replaced by $k + 1$.

Using $\alpha = 10$, 20, 30 and 50%, we have done a number of tests to chose a proper α. It turns out that $\alpha = 50\%$ produces the best result over the ocean. The threshold retracking works well if the waveform contains just one ramp. However, if the waveforms contain more than one ramp, the retracking gate is determined in favor of the leading edge of the first ramp, which may not correspond to the ocean returns and could lead to a false result. Therefore, we modify the threshold retracking algorithm to resolve this problem in Section 3.2.

3.2 Improved threshold retracking

In the case of complex waveforms, the threshold retracker cannot properly determine the center of the leading edge. As such, we present an improved threshold retracker. Figure 4 shows a flowchart of the improved threshold retracker, which determines one or more sub-waveforms and retracking gates, and then selects a best retracking gate according to the following procedure.

First, the difference between the powers of every other two gates is computed. If half of the difference is greater than a given value ε_1, then it shows that the antenna begins to pick up the returning power. In this case (difference $> \varepsilon_1$), the difference between two successive powers is computed. If this difference is greater than another given value ε_2, then it indicates that the antenna continues to pick up the returning power, and the corresponding gate and power are included in the first sub-waveform. The selection of sub-waveform gates is terminated when the difference is smaller than ε_2. Both ε_1 and ε_2 are determined empirically, and we found that the result with $\varepsilon_1 = 8$, and $\varepsilon_2 = 2$ is the best.

The sub-waveform is then extended by including four gates at the beginning and the end of the sub-waveform. Using the selected samples in the sub-waveform, a retracking gate corresponding to this sub-waveform is determined using Eqs. (7), (11), (12) and (13). This process is repeated for the next sub-waveform and a new retracking gate is determined.

At the final step, we compare the previous SSH with the current SSHs associated with the computed retracking gates to make decision: the "best" retracking gate is the one that yields the smallest difference between the current SSH and the previous SSH. If use of the previous SSH results in a large gradient, the earlier SSH is chosen. Since it is more likely that the SSH can be accurately determined in the open ocean than in the coastal waters, we always start the retracking from the open ocean and then proceed to the land. This is to ensure the criterion of SSH for the "best" retracking gate works properly.

As a numerical example of the improved threshold retracker, Fig. 5 shows a corrupted waveform of Geosat/GM over Peng-Hu Island (at about 23.5°N, 119.5°E) in the Taiwan Strait. In Fig. 5, there are two leading edges (ramps) in the waveform. Clearly the pre-defined tracking gate is not at either of the center points of the two leading edges. The improved threshold retracker determines the two retracking gate (24 and 32) of the two sub-waveforms first. Two retracking-corrected SSHs are then compared with the previous SSH to obtain the best retracking gate, which is 24 in this case.

3.3 Results of waveform retracking around Taiwan

We have experimented with waveform retracking around Taiwan using the retrackers described earlier. One important issue is to find the optimal retracker for the subsequent gravity anomaly derivation. The selection of such a retracker is based on the following two criteria

1. Success rate of retracking, and
2. The standard deviation of the differences between the retracked SSHs and modeled geoid heights.

The geoid model for use in Criterion 2 is a gravimetric geoid model of Taiwan computed from the latest land/marine gravity data and airborne gravity data (C. Hwang et al., submitted). Because of the crude assumption made in the OCOG retracker, the OCOG is only used for computing a priori values of the parameters needed in the other retrackers. Table 1 compares retracked SSHs and geoidal heights along Geosat/GM tracks 85206 and 85282 (Fig. 2). In Table 1, we list the number of successfully retracked waveforms, the

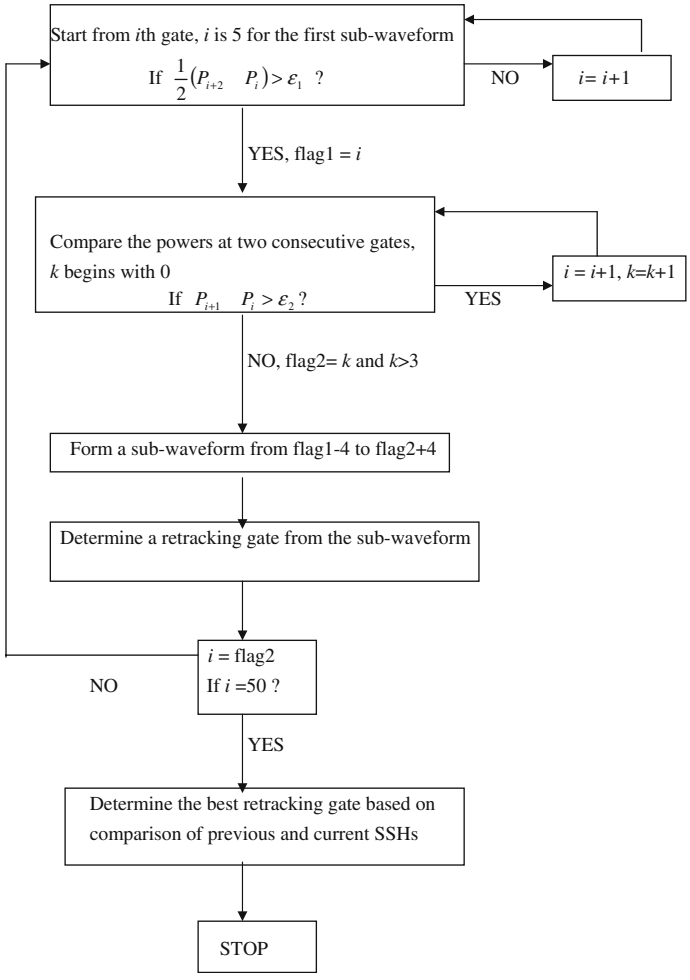

Fig. 4 Flow chart of the improved threshold retracking

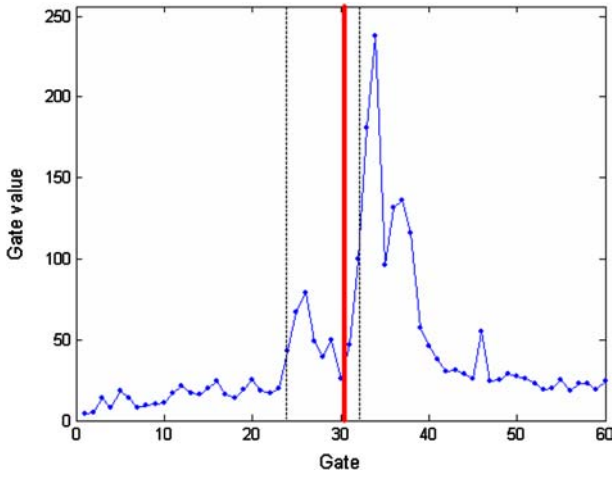

Fig. 5 A corrupted waveform over Peng-Hung Island and the two retracking gates (24 and 32) from the improved threshold retrackers, corresponding to two sub-waveforms. The theoretical tracking gate is 30.5

number of raw waveforms, the ratio between these two numbers and the standard deviation of the differences between retracked SSHs and geoidal heights for each retracker. Because of the complex waveforms near the coasts, the success rate of the Beta-5 retracker is only 70%. There is no problem of convergence for the threshold retracker, so its success rate is always 100%. The improved threshold retracker yields almost 100% success rate. The standard deviations of the height differences in Table 1 are based on only retracked SSHs.

Table 1 Statistics of waveform retracking for two geosat/GM tracks

Retracker	Total no.	Processed no.	Ratio (%)	Standard deviation of difference[a] (m)
(a) Track 85206				
Beta-5	285	201	70.5%	0.48
Threshold	285	285	100.0%	0.46
Improved threshold	285	283	99.3%	0.26
(b) Track 85282				
Beta-5	172	130	75.6%	0.31
Threshold	172	172	100.0%	0.36
Improved threshold	172	171	99.4%	0.19

[a] Difference between retracked SSH and geoidal height

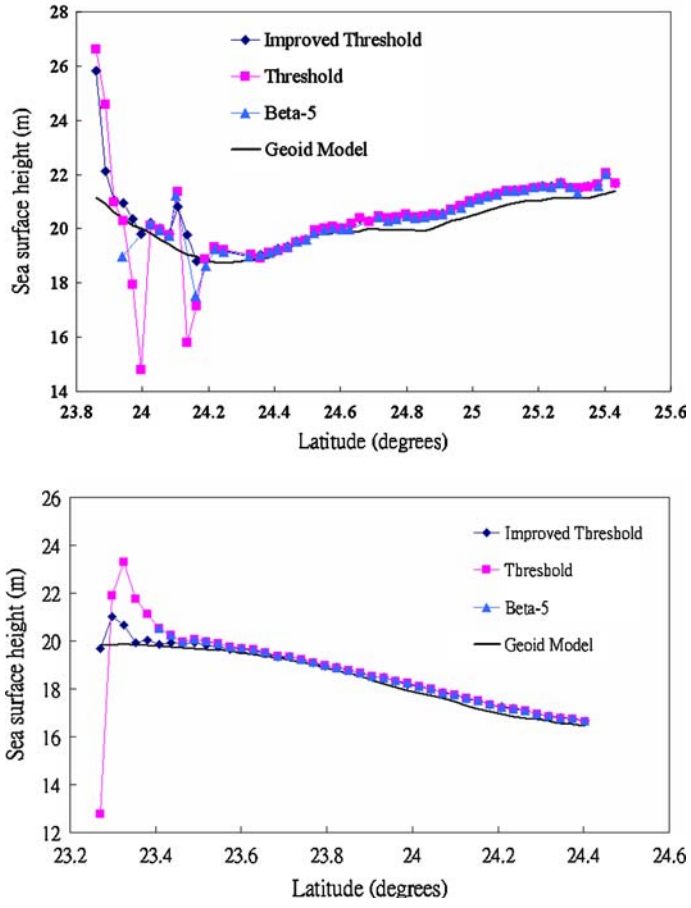

Fig. 6 Comparison of raw and retracked SSHs along Geosat/GM tracks 85206 and 85282

Figure 6 compares SSHs from various retrackers with geoidal heights. In general, the deviation of SSH from geoidal height increases as the tracks approach the land. On average, the Beta-5 retracker delivers success rates of retracking at about 70–80 % but fails for remaining waveforms in areas closer to the coastline. Therefore, the Beta-5 retracker is considered inadequate for retracking around Taiwan. In terms of both success rate and standard deviation, Table 1 shows that the improved threshold retracker is significantly better than the other two retrackers. The results from other altimeter tracks confirm that the improved threshold retracker indeed outperforms the other two retrackers, and hence it is selected as the optimal retracker in this paper.

The improved threshold retracker is further tested considering the dependency of retracking accuracy on region and depth. Figure 7 shows the ground tracks of retracked SSHs around Taiwan, totaling 165 Geosat/GM tracks. The performance of the improved threshold retracker is assessed at four marine zones in Fig. 6 and at regions of different distances to the shores. Figure 8 shows the distribution of the differences between retracked SSHs and geoidal heights. As seen in Fig. 8, retracking not only improves the accuracy of SSH over the coastal waters, but also over the open ocean. The places with most improved SSHs are near islands in the ocean and around barrier islands off the west coast of Taiwan.

However, it is clear that not all SSHs can be properly corrected by retracking, as large errors remain in Fig. 8. This is a limitation of waveform retracking. Some of the large errors may be caused by improper retracking and/or tide model error. At the central Taiwan Strait off the coasts of the mainland China and Taiwan, the tidal amplitude can reach 3 m. As an example, we computed the amplitudes and phase of the M2 tide at the Hsinchu tide gauge station (at about 24.80°N, 120.96°E) from the tide gauge records and from the CSR4.0 tide model. The differences in amplitude and phase are 0.50 m and 22°, respectively. Compared to the Taiwan Strait, tide model error in the Pacific Ocean east of Taiwan will be smaller, since the latter is over the deep open oceans (Fig. 1). Efforts beyond waveform retracking for improving altimetry quality are presented in Anzenhofer et al. (1999).

The improvement percentage (IMP) of retracked SSHs is also computed, using

$$\mathrm{IMP} = \frac{\sigma_{\mathrm{raw}} - \sigma_{\mathrm{retracked}}}{\sigma_{\mathrm{raw}}} \times 100\% , \tag{14}$$

where σ_{Raw} and $\sigma_{\mathrm{Retracked}}$ are the standard deviations of the differences between raw SSHs and geoidal heights, and retracked SSHs and geoidal heights, respectively. Table 2 shows the improvement percentages in four cases. A negative improvement percentage indicates that retracking deteriorates

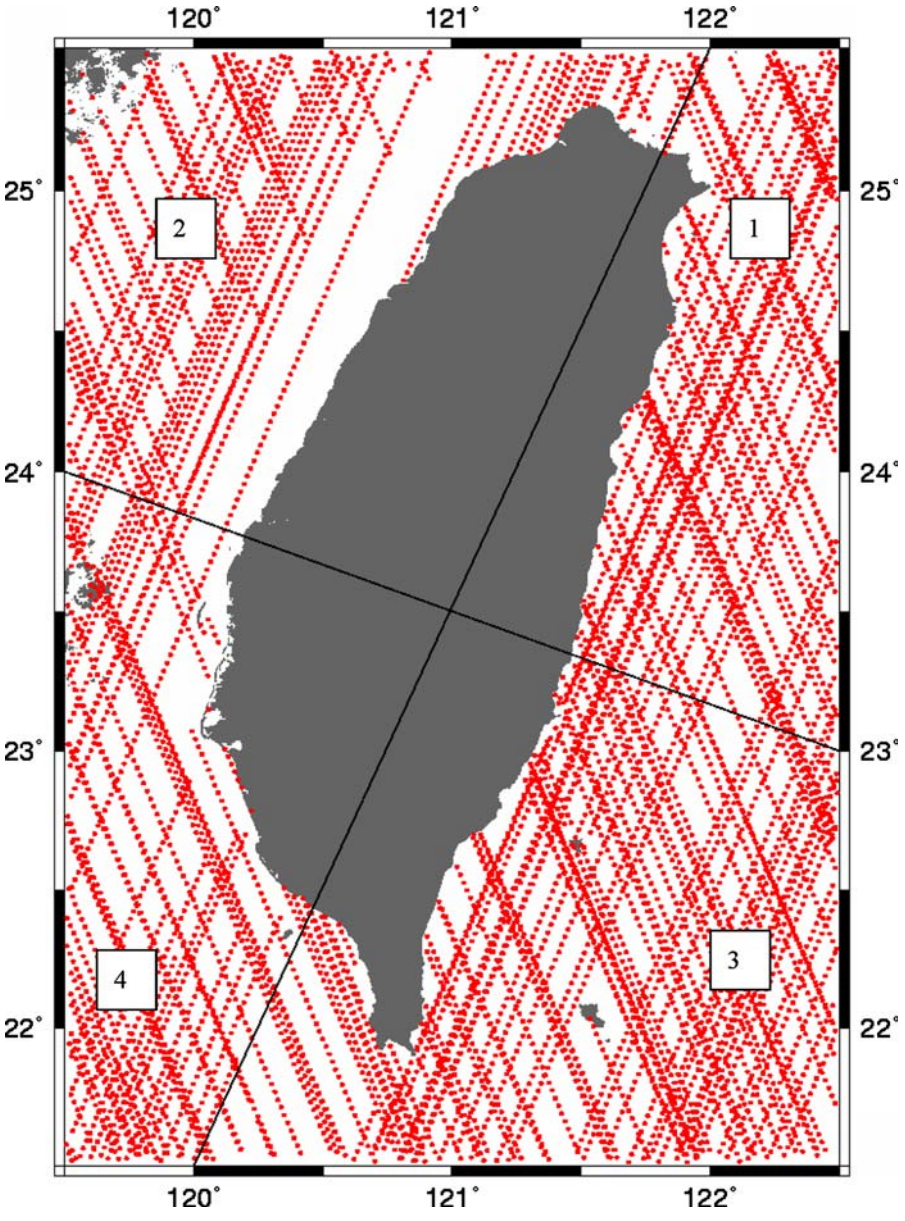

Fig. 7 Distribution of Geosat/GM ground tracks and four zones of comparison

the SSHs. Table 2 shows that the improvement percentage increases as the water approaches land. While the difference in the improvement percentage between the marine zones at 20 and 10 km to the shores is only marginal, the difference in standard deviation is significant. The largest improvement is at Zone 1 and the least improvement is at Zone 4, irrespective of the distance to the shore.

The improvement percentage at Zone 2 is −3.5% and this value is explained as follows. First, the fact that Zone 2 contains only a few SSHs near the coasts (Fig. 7) makes the statistics of improvement percentage unreliable, because the major improvement of SSH accuracy by retracking occurs near the coasts. The standard deviations of the differences for the case of raw SSHs and the case of retracked SSHs are 0.534 and 0.553 m, respectively. Given the size of the SSH error (about 0.5 m, Table 2), such a marginal difference (1.9 cm) is statistically insignificant. The SSHs used in the following gravity anomaly derivations are based on the retracking corrections from the improved threshold retracker.

4 Gravity anomalies from retracked Geosat/GM altimetry

4.1 Gravity anomaly derivation by least-squares collocation

We have experimented with two methods of gravity derivation from retracked SSHs of Geosat/GM. One is the inverse Vening Meinesz formula (Hwang 1997) and the other is least-squares collocation (LSC) (Moritz 1980; Hwang and

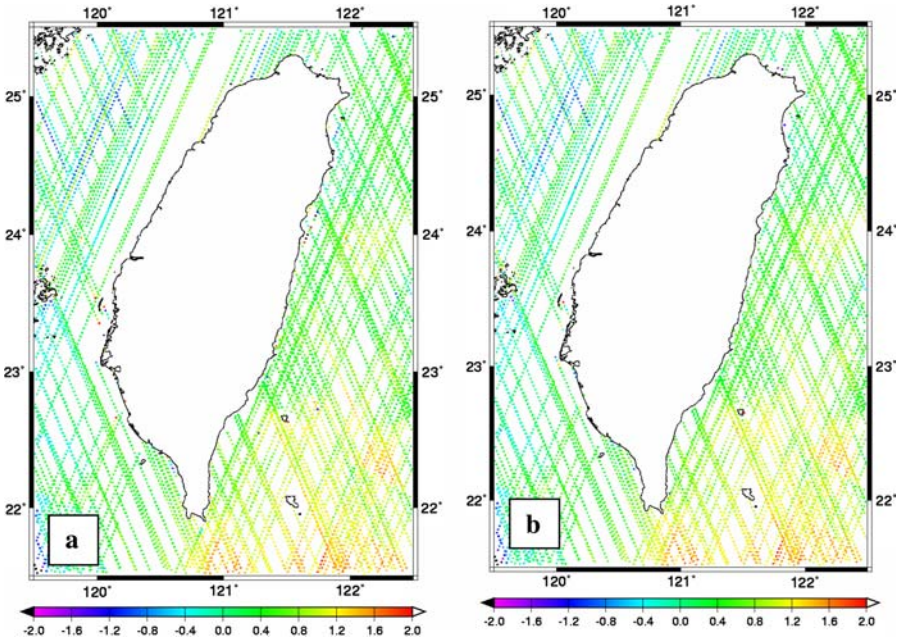

Fig. 8 Distributions of differences **a** between raw SSH and geoidal heights, and **b** between retracked SSH and geoidal heights

Table 2 Standard deviation of differences between raw SSH, retracked SSH and geoidal heights and improvement percentage (IMP)

Area of comparison	Raw (m)	Retracked (m)	IMP (%)
(a) Case 1: IMP as a function of distance to shore			
All	0.744	0.686	7.8
Area within 20 km of shore	1.274	1.060	16.8
Area within 10 km of shore	1.920	1.581	17.7
Zone	Raw (m)	Retracked (m)	IMP (%)
(b) Case 2: IMP as a function of zone			
1	0.603	0.477	20.9
2	0.534	0.553	−3.5
3	0.560	0.515	8.0
4	0.989	0.873	11.7
(c) Case 3: IMP as a function of zone and distance (20 km) to shore			
1	1.284	0.95	26.0
2	0.624	0.5	19.8
3	0.856	0.72	15.8
4	2.112	1.813	14.1
(d) Case 4: IMP as a function of zone and distance (10 km) to shore			
1	2.009	1.476	26.5
2	0.828	0.625	24.5
3	1.358	1.119	17.6
4	2.819	2.435	13.6

Parsons 1995). In all experiments (Section 4.2), the LSC always outperforms the inverse Vening Meinesz formula by few mgal in the accuracy of computed gravity anomaly. Thus, gravity derivations in Section 4.2 will be solely based on LSC. Furthermore, the LSC is able to combine heterogeneous data for gravity anomaly derivation and this function is needed in our experiments. In all cases, the sea surface topography (SST) is regarded as zero, so that SSH is considered identical to geoidal height. In fact, there is no reliable estimate of SST around this region.

We used the standard remove–restore procedure in the LSC derivation of gravity anomalies. The along-track geoid gradient derived from the SSH is used as the data type. The adopted reference gravity field is a combined gravity field from the GRACE GGM02C model (degrees 2 to 200, http://www.csr.utexas.edu/grace/; Tapley et al. 2005) and the EGM96 model (degrees 201 to 360; Lemoine et al. 1998). First, a residual geoid gradient is computed by

$$e_{\text{res}} = e - e_{\text{long}} \tag{15}$$

where e, e_{long} and e_{res} are observed, long-wavelength and residual gradients, respectively.

The residual gravity anomaly is computed by the standard LSC formula with geoid gradients as input (Hwang and Parsons 1995):

$$\Delta g_{\text{res}} = \mathbf{C}_{\Delta \mathbf{ge}}(\mathbf{C}_{\mathbf{ee}} + \mathbf{C}_{\mathbf{nn}})^{-1}\mathbf{e}_{\mathbf{res}} \tag{16}$$

where $\mathbf{e_{res}}$ is a vector of residual geoid gradients, $\mathbf{C}_{\Delta \mathbf{ge}}\mathbf{C}_{\mathbf{ee}}$, and $\mathbf{C_{nn}}$ are covariance matrices for gravity anomaly–gradient, gradient–gradient and noise of gradient, respectively.The $\mathbf{C_{nn}}$ is a diagonal matrix holding the noise variances of geoid gradients. Based on numerous tests, it was found that a noise variance of $4\,\text{s}^2$ for geoid gradient produces the best gravity anomalies.

In the case of using combined altimeter and airborne gravimeter data, a residual gravity anomaly is computed by

$$\Delta g_{\text{res}} = (\mathbf{C}_{\Delta \mathbf{g}\Delta \mathbf{g}_\mathbf{a}}\ \mathbf{C}_{\Delta \mathbf{ge}}) \begin{pmatrix} \mathbf{C}_{\Delta \mathbf{g}_{\mathbf{ar}}} + \mathbf{C}_{\mathbf{mm}} & \mathbf{C}_{\Delta \mathbf{g}_\mathbf{a}\mathbf{e}} \\ \mathbf{C}_{\mathbf{e}\Delta \mathbf{ga}} & \mathbf{C}_{\mathbf{ee}} + \mathbf{C}_{\mathbf{nn}} \end{pmatrix}^{-1} \begin{pmatrix} \Delta \mathbf{g}_{\mathbf{ar}} \\ \mathbf{e}_{\mathbf{res}} \end{pmatrix} \tag{17}$$

where $\Delta \mathbf{g_{ar}}$ is a vector of residual airborne gravity anomalies, $\mathbf{C}_{\Delta \mathbf{g}_\mathbf{a}\mathbf{e}}$, $\mathbf{C}_{\mathbf{e}\Delta \mathbf{ga}}$, and $\mathbf{C}_{\Delta \mathbf{g}\Delta \mathbf{g}_\mathbf{a}}$ are covariance matrices for airborne gravity anomaly–gradient, gradient–gravity anomaly, and gravity anomaly–airborne gravity anomaly, respectively, and $\mathbf{C_{mm}}$ is a diagonal matrix holding the noise variances of airborne gravity anomalies. In this paper, a noise variance of $9\,\text{mgal}^2$ is used in $\mathbf{C_{mm}}$ (C. Hwang et al. submitted).

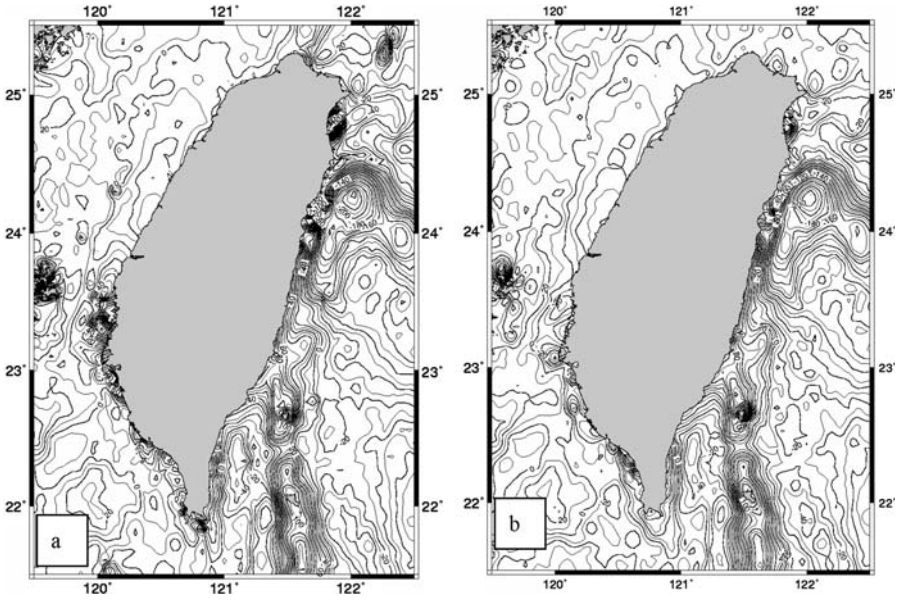

Fig. 9 Contours of gravity anomalies using **a** raw SSH, and **b** retracked SSH

The LSC method in Eq. (17) combines downward continuation, altimeter-to-gravity conversion and interpolation in one step using proper covariance functions. All the needed covariance functions and matrices were constructed based on the error degree variances of the combined GGM02C–EGM96 gravity field and the Tscherning and Rapp (1974) Model 4 degree variance; see Hwang and Parsons (1995, Appendix A) for the detail of covariance modeling related to this work.

4.2 Results: comparison with shipborne and airborne gravity data

The purpose of experiments in this section is to see whether retracking improves the accuracy of altimeter-derived gravity anomaly and to see the role of airborne gravity data. We computed three sets of gravity anomalies (designated as computed gravity anomaly) by LSC using the following three data sets:

Data set 1: raw SSHs,
Data set 2: retracked SSHs, and
Data set 3: retracked SSHs and airborne gravity anomalies.

The resulting gravity anomalies from the three data sets were then compared with shipborne gravity anomalies. The gravity anomalies derived from Data sets 1 and 2 were also compared with airborne gravity anomalies at the flight altitude (5,156 m).

The shipborne gravity anomalies are from Hsu et al. (1998) and have been carefully edited and crossover adjusted. The estimated uncertainties of the shipborne gravity anomalies depend on ship cruises and locations, and are about a few mgal (Hsu et al. 1998). The airborne gravity anomalies are from C. Hwang et al. (submitted) and were collected at an average altitude of 5,156 m using a LaCoste and Romberg System II air/sea gravimeter. Based on the crossover analysis of C. Hwang et al. (submitted), the estimated uncertainty of airborne gravity anomalies is about 3 mgal. The airborne gravity data were mostly collected along north–south and west–east oriented lines, which are spaced at 4.5 and 20 km, respectively (Fig. 10). Note that the gravity signal at an altitude of 5,156 m is attenuated and its spectral content is different from that at sea level.

Table 3 shows the statistics of the differences between the computed gravity anomalies (three data sets) and the shipborne gravity anomalies. As another independent assessment, Table 4 shows the statistics of the differences between the computed gravity anomalies (data sets 1 and 2) and the airborne gravity anomalies. For comparison with airborne gravity anomalies, the altimeter-derived gravity anomalies were upward continued to the flight altitude (5,156 m) using a remove–restore procedure with the long-wavelength part from the combined GGM02C and EGM96 gravity field, see also C. Hwang et al. (submitted). To enhance the accuracy of the upward continuation, the land gravity anomalies on Taiwan were incorporated with the altimeter-derived gravity anomalies.

Both Tables 3 and 4 show that the use of retracked SSHs indeed improves the accuracy of gravity anomalies. The percentage of improvement by retracking in this case is 11%. Adding airborne gravity to retracked SSHs further improves the accuracy, and the improvement is about 1 mgal. Possible reasons for such a marginal improvement (only 1 mgal) are (1) airborne gravity data provide additional information only at the wavelengths corresponding to the flight altitude, and (2) downward continuation enlarges the noise of airborne gravity anomalies at sea level. As such, the resulting gravity anomalies from combined altimetry and airborne data cannot achieve the same accuracy as the airborne gravity anomalies (3 mgal at the flight altitude).

Figure 9 shows gravity anomalies derived from raw SSHs and retracked SSHs. Many gravity artifacts associated with

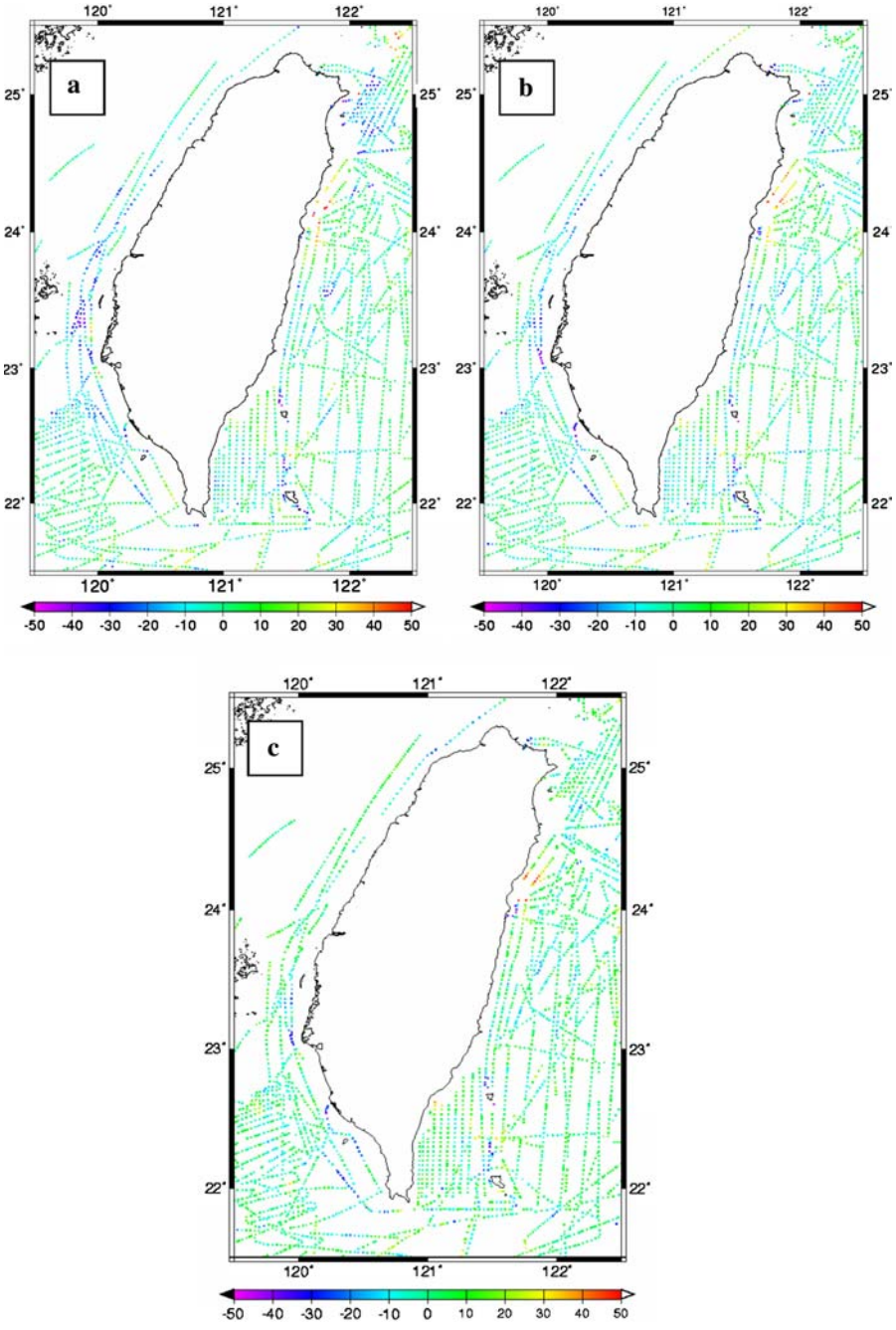

Fig. 10 Distributions of differences between altimeter-derived and shipborne gravity anomalies, **a** raw SSH, **b** retracked SSH, and **c** retracked SSH and airborne gravity

the raw SSHs (Fig. 9a) have disappeared in the gravity field associated with the retracked SSHs (Fig. 9b). Examples of such changes can be found at, e.g., a location northeast of Taiwan (here many islands exist) and a marine zone near Peng-Hu Island (central Taiwan Strait) and the waters off the southwest coast of Taiwan. This pattern of gravity accuracy improvement is consistent with the pattern of SSH accuracy improvement (Fig. 8). Furthermore, there are locations with gravity artifacts in the gravity field derived from the retracked SSHs, and these are coincident with large remaining errors in the retracked SSHs (Fig. 8b).

Figure 10 shows the distribution of the differences between computed gravity anomalies (three data sets) and shipborne gravity anomalies. The differences in Fig. 10a, 10b are consistent with the differences in Fig. 9a, 9b. These differences show the regions where SSHs receive corrections from retracking and the accuracy of gravity anomalies is improved. In Fig. 10b, some of the differences off the east coast

Table 3 Statistics of differences (mgal) between shipborne and altimeter-derived gravity anomalies

Data	Max	Min	Mean	Standard deviation
Raw SSH	143.22	−114.26	−1.56	13.48
Retracked SSH	137.83	−112.329	−0.91	11.98
Retracked SSH+ airborne gravity	130.09	−109.32	1.59	11.05

Table 4 Statistics of differences (mgal) between airborne (at sea only) and altimeter-derived gravity anomalies at the flight level

Data	Maximum	Minimum	Mean	Standard deviation
Raw SSH	79.90	−45.65	3.79	10.34
Retracked SSH	79.31	−54.61	3.62	9.86

of Taiwan at about 24.3°N exceed 50 mgal. Here use of a better retracker than the improved threshold retracker is needed to correct for the errors, or these retracked SSHs will have to be removed.

The differences in Fig 10b, 10c show the effects of including airborne gravity data. Adding airborne gravity to retracked SSHs improves the accuracy of gravity anomalies at marine zones close to, but not limited to, the coasts. The area with the most improved accuracy is over the waters off the entire west coast of Taiwan, and the waters around the islands in the Pacific Ocean. The location with excessively large errors in the altimeter-only gravity anomalies (at 24.3°N off the east coast of Taiwan) also sees some reduction in the error by adding the airborne gravity data, but unfortunately some errors are enlarged (probably due to downward continuation).

Figure 11 shows the distribution of the differences between computed gravity anomalies (data sets 1 and 2) and airborne gravity anomalies. Here, we will just discuss the differences at sea because altimeter data are available only at sea. The difference between the computed and the airborne gravity anomalies is a function of location, altimeter data density (Fig. 7), retracking quality (Fig. 8), and roughness of gravity (Fig. 1). The pattern of improvement of gravity anomaly accuracy by retracking in Fig. 11 is similar to that in Fig. 10, but Fig. 11 shows more detail of improvement in the immediate vicinity of the coasts and islands. Figure 11b shows that, as in Fig. 10b, there are remaining large errors in altimeter-derived gravity anomalies even when retracked SSHs are used. Therefore, for coastal gravity anomaly derivation, the best strategy will be to remove erroneous SSHs and then fill the gap with airborne gravity data.

5 Conclusions

This paper assesses the performances of three waveform retrackers and presents an improved threshold retracker, which is considered the optimal one for the area under study. Waveform retracking has improved the accuracy of Geosat/GM altimetry, but the improvement is limited to the cases when the waveforms can be properly retracked. As such, some of the retracked SSHs still contain large errors that damage the results of their applications. Such remaining large errors normally occur over the waters around islands and in the immediate vicinity of the coast. Despite these limitations, retracking has been shown to improve the accuracy of Geosat/GM-derived gravity anomalies. Again, the extent of accuracy improvement of gravity is limited by the effectiveness of retracking. Inclusion of airborne gravity data to retracked Geosat/GM altimetry further improves gravity accuracy, especially over coastal waters.

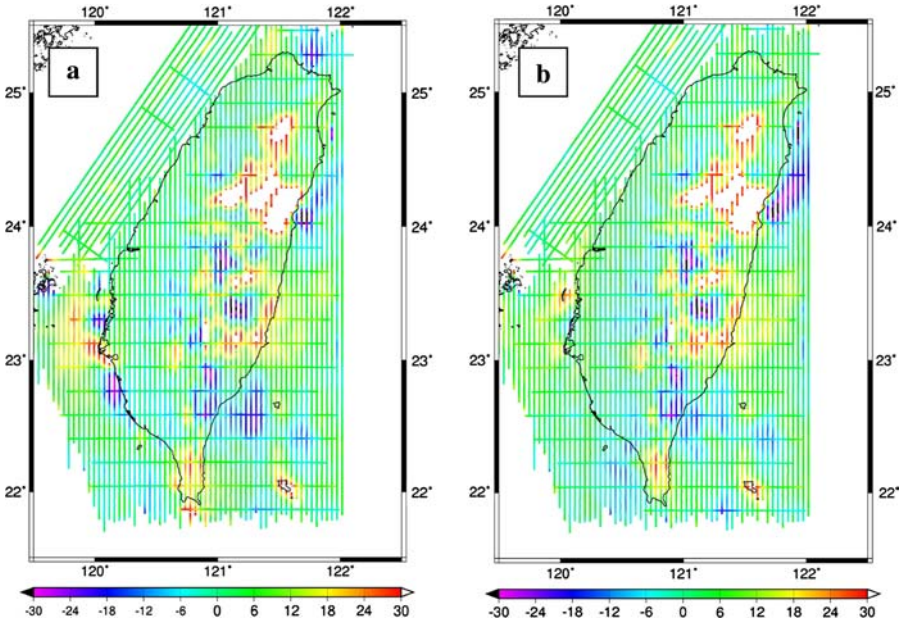

Fig. 11 Distributions of differences between altimeter-derived and airborne gravity anomalies, **a** raw SSH, and **b** retracked SSH

There are other factors than waveform contamination that will affect the accuracy of altimeter-derived SSH (Anzenhofer et al. 1999). One important factor is tide model error. Applying bad tidal corrections to properly retracked SSHs will surely damage the results of altimetry applications. Thus, important future work is to use retracked altimetry to improve tide models, especially around coastal waters. The ideal altimeter data for such work are not Geosat/GM data, but repeat altimeter data from such missions as Geosat/ERM, ERS-1/2, TOPEX/Poseidon and Envisat, all requiring waveform retracking before use.

Acknowledgements This research is supported by the National Science Council, Taiwan, under grants no. NSC-93-2611-M-009-001 and NSC-92-2211-E-009-047, and the Ministry of the Interior, Taiwan. We thank John Lillibridge for supplying the Geosat/GM waveforms. This is a contribution to International Association of Geodesy Study Group 2.3 (2003–2007).

References

Andersen OB, Knudsen P, Berry PAM, Mathers L, Trimmer R, Kenyon S (2005) Initial results from retracking and reprocessing the ERS-1 geodetic mission altimeter for gravity field purposes. In: Sansò F (ed) A window on the future of Geodesy. Springer, Berlin Heidelberg New York, pp 1–5

Anzenhofer M, Shum CK, Rentsh M (1999) Coastal altimetry and applications. Rep. 464, Dept Geod Sci and Surveying, Ohio State University, Columbus

Brown GS (1977) The average impulse response of a rough surface and its applications. IEEE Trans Ant Prop AP-25(1):67–74

Cheney RE, Emery WJ, Haines BJ, Wentz F (1991) Recent improvements in GEOSAT altimeter data, EOS – Trans AGU 72(51):577–580

Cole TD (1985) Geosat-A data users/ground system interface control document (ICD), 7292–9510 REV.1, Applied Physics Lab, Johns Hopkins University

Davis CH (1997) A robust threshold retracking algorithm for measuring ice-sheet surface elevation change from satellite radar altimeter. IEEE Trans Geosci Remote Sens 35(4):974–979

Deng XL, Featherstone WE, Hwang C, Berry PAM (2002) Estimation of contamination of ERS-2 and POSEIDON satellite radar altimetry close to the coasts of Australia. Mar Geod 25(4): 249–271, doi 10.1080/01490410290051572

Deng X (2004) Improvement of geodetic parameter estimation in coastal regions from satellite radar altimetry. PhD Thesis, Curtin University of Technology

Fu LL, Cazenave A (2001) Satellite altimetry and earth sciences: a handbook of techniques and applications. Academic, San Diego

Hsu S, Liu C, Shyu C, Liu S, Sibue J, Lallemand S, Wang C, Reed D (1998) New gravity and magnetic anomaly maps in the Taiwan–Luzon region and their preliminary interpretation. Terr Atm Ocean 9(3):509–532

Hwang C (1997) Analysis of some systematic errors affecting altimeter-derived sea surface gradient with application to geoid determination over Taiwan. J Geod 71(2):113–130

Hwang C, Parsons B (1995) Gravity anomalies derived from SEASAT, GEOSAT, ERS-1 and TOPEX/Poseidon altimeter and ship gravity: a case study over the Reykjanes Ridge. Geophys J Int 122:551–568

Hwang C (1998) Inverse Vening Meinesz formula and deflection-geoid formula: applications to the predictions of gravity and geoid over the South China Sea. J Geod 72:304–312

Hwang C, Hsu HY, Jang RJ (2002) Global mean sea surface and marine gravity anomaly from multi-satellite altimetry: applications of deflection-geoid and inverse Vening Meinesz formulae. J Geod 76:407–418

Jan S, Chern CS, Wang J, Chao SY (2004) The anomalous amplification of M-2 tide in the Taiwan Strait. Geophys Res Lett 31(7): Art. no. L07308

Lemoine, FG, Kenyon SC, Factor JK, Trimmer RG, Pavlis NK, Chinn DS, Cox CM, Klosko SM, Luthcke SB, Torrence MH, Wang YM, Williamson RG, Pavlis EC, Rapp RH, Olson TR (1998) The Development of Joint NASA GSFC and the National Imagery and Mapping Agency (NIMA) Geopotential Model EGM96. Rep NASA/TP-1998–206861, National Aeronautics and Space Administration, Greenbelt

Lillibridge JL, Smith WHF, Scharroo R, Sandwell DT (2004) The Geosat geodetic mission twentieth anniversary edition data product. AGU 2004 Fall meeting, San Francisco

Martin TV, Zwally HJ, Brenner AC, Bindschadler RA (1983) Analysis and retracking of continental ice sheet radar altimeter waveforms. J Geophys Res 88:1608–1616

Mathers L, Berry PAM, Freeman JA (2004) Gravity, geoid and space missions. IAG international symposium, Porto, August–3- September 2004

Moritz H (1980) Advanced physical geodesy. Abacus Press, New York

Smith WHF, Sandwell DT (2004) Improved global marine gravity field from reprocessing of Geosat and ERS-1 radar altimeter waveforms. AGU 2004 Fall meeting, San Francisco.

Tapley BD, Ries J, Bettadpur S, Chambers D, Cheng M, Condi F, Gunter B, Kang Z, Nagel P, Pastor R, Pekker T, Poole S, Wang F (2005) GGM02 – An improved Earth gravity field model from GRACE. J Geod 79:467–478

Tscherning CC, Rapp RH (1974) Closed expressions for gravity anomalies, geoid undulations and deflection of the vertical implied by anomaly degree variance models. Rep 208, Dept Geod Sci and Surveying, Ohio State University, Columbus

Wingham DJ, Rapley CG, Griffiths H (1986) New techniques in satellite tracking system. In: Proceedings of IGARSS' 88 symposium, Zurich, pp 1339–1344

Zwally HJ, Brenner AC (2001) Ice Sheet dynamics and mass balance, in Fu LL, Cazenave A (eds) satellite altimetry and earth sciences: a handbook of techniques and applications. Academic San Diego, pp 351–369